

Supplementary materials

Enhanced sieving of cellulosic microfibers membranes via tuning of interlayer spacing

Zoheb Karim^{1,2,*}, Susanna Monti^{3*}, Giovanni Barcaro⁴, Anna Svedberg¹, Mohd Ayub Ansari⁵, Sadaf Afrin⁶

¹MoRe Research Örnköldsvik AB, Box 70, SE-89122, Örnköldsvik, Sweden

²Institute of Architecture and Civil Engineering, South Ural State University, Chelyabinsk, 454080, Russia

³CNR-ICCOM– Institute of Chemistry of Organometallic Compounds, via Moruzzi 1, 56124 Pisa, Italy

⁴CNR-IPCF–Institute for Chemical and Physical Processes, via Moruzzi 1, 56124 Pisa, Italy

⁵Department of Chemistry, Bipin Bihari College, 284001, Jhansi, India

⁶Department of Chemistry, Faculty of Chemical Sciences, Aligarh Muslim University, Aligarh 202002, India

Corresponding authors: Z.K (zoheb.karim@gmail.com)

S.M (sapeptides@gmail.com)

Table of content:

S.No	Sections	
1.	Materials	
2.	Functionalization of cellulose microfibers (CMF)	
	2.1.	TEMPO oxidation
	2.2.	Phosphorylation
	2.3.	Methylation
3.	Fabrication of nanolamnated membranes	
4.	Characterization of membranes	
	4.1.	Scanning Electron Microscopy (SEM)
	4.2.	Surface ζ -potential measurement
	4.3.	Quantitative analysis of functional groups
	4.3.1	Carboxylic
	4.3.2.	Phosphate
	4.3.3.	Methyl
	4.4.	Infrared spectroscopy
	4.5.	^{13}C CP MAS and ^{31}P MAS NMR spectroscopy
	4.6.	XRD analysis
	4.7.	XPS analysis of functionalized CMF
	4.8.	Water permeability
	4.9	Molecular weight cut-off (MWCO)
	4.10.	BET measurement
	4.11.	Mechanical properties and air permeance
5.	Nanolaminated membranes performance	
	5.1.	Ions permeation rate
	5.2.	Membrane performance for removal of metal ions, dye and drugs
	5.3.	Long term stability analysis
6.	Comparative study with literature	
7.	Model building and simulation details	
8.	References	

1. Materials:

Cellulose microfibers (CMF) (Exilva P 01-V) was supplied by Borregaard AB (Sarpsborg, Norway). The charge density of CMF was $28.54 \pm 4.09 \mu\text{mole/g}$ and dry weight concentration was 9.3 wt%. Enzyme hexokinase was purchased from Novozymes, USA. 2,2,6,6-tetramethyl-1-piperidinyloxy (TEMPO) and all other chemicals used in this study were purchased from Sigma Aldrich, USA. Chemicals (analytical grade) were used without any further purification.

2. Functionalization of Cellulose microfibers (CMF): CMF were functionalized using chemicals and enzyme hexokinase and denoted functional groups were introduced on the surface of CMF.

2.1. TEMPO oxidation: CMF suspension was oxidized as discussed by Serra et al.¹. In a typical experiment, 15 g of CMF were dispersed in distilled water containing previously dissolved TEMPO (0.0156 g per g of MFC) and NaBr (0.1 g per g of CMF). The mixture was stirred for 15 min in order to assure good dispersion of all the substances. After mix, a 3.0, 6.0 and 10.0 ml of 10 wt% NaClO solution was added to the slurry. The pH was kept at 10 by addition of 0.5 M NaOH solution. The oxidized CMF were then filtered and washed with Milli-Q water and stored for further use.

2.2. Phosphorylation: Surface modification of CMF (1 wt%) using enzyme hexokinase was performed as discussed by Bozic et al.² Briefly, reaction proceeds in 1 wt% of CMF in phosphate buffer (pH 7.6) in the presence of a 50 mM ATP, 50, 100 and 200 mM of MgCl_2 and 35 U ml^{-1} of enzyme for 24 h at 30 °C.

2.3. Methylation: CMF (1 wt%) was mercerized using 60 mL NaOH solution (50% m/v) for 1 h at room temperature. The excess NaOH was removed by filtration and acetone (27.0 mL) was added as a solvent. Dimethyl sulfide (DMS) (9.0 mL) was added drop-wise and the reaction was carried out at 50 °C. After 1 h of reaction, the system was filtered and fresh reagents were added (acetone and DMS), maintaining the same previous proportions. At the end, the sample was neutralized using acetic acid (10% v/v), filtered, and washed with acetone (three times with 90 mL) and finally dried in an oven at 50 °C for 6 h. The synthesis process was adapted from Vieira et al.³.

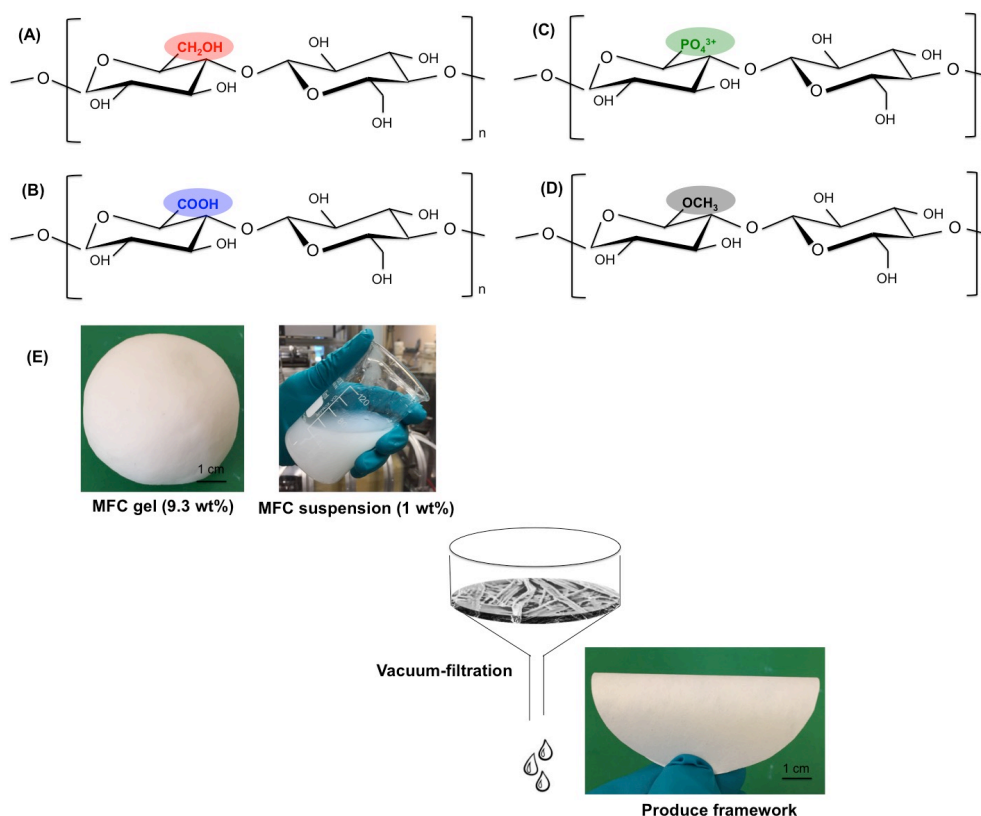


Figure S1: Introduction of functional groups on C6 carbon of cellulose monomer after functionalization of CMF. **A**, pristine-CMF having hydroxyl (-OH) group on C6. **B**, TEMPO functionalization of CMF introduced carboxylic (-COOH) group on CMF. **C**, phosphorylation of CMF using enzyme hexokinase and introduce phosphate (PO_4^{3-}) group on CMF. **D**, Methylation of CMF and introduced methyl hydrophobic group (CH_3). **E**, Nanolaminate membranes were produced using very simple and scalable technique, vacuum-filtration. The 1 wt% of CMF suspension (150 ml) was filtered using funnel. It is worth mentioning that except methyl groups all three groups are hydrophilic in nature.

3. Fabrication of nanolaminate membranes:

2D membranes were fabricated using vacuum filtration. Total 150 ml of pristine and functionalized CMF suspensions (1wt % each) was filtered using a Buchner funnel setup (600 ml of volume capacity). After the draining off of the water, the filtered frameworks were removed from the Buchner funnel and dried at room temperature for 48 h and whatman papers were replaced after each 10 h for fast drying. Produced frameworks (12.5 cm in diameter) were denoted as pristine-CMF, carboxylic-CMF,

phosphate-CMF and methyl-CMF nanolaminate membranes with respect to their introduced functional groups (**Figure S1E**).

4. Characterization of membranes:

4.1. Scanning Electron Microscopy (SEM):

The membranes sputter coated with tungsten were observed in the SEM (MAGELLAN 400, SEM, FEI Company) at an acceleration voltage of 3 kV to understand the morphology and nanostructure.

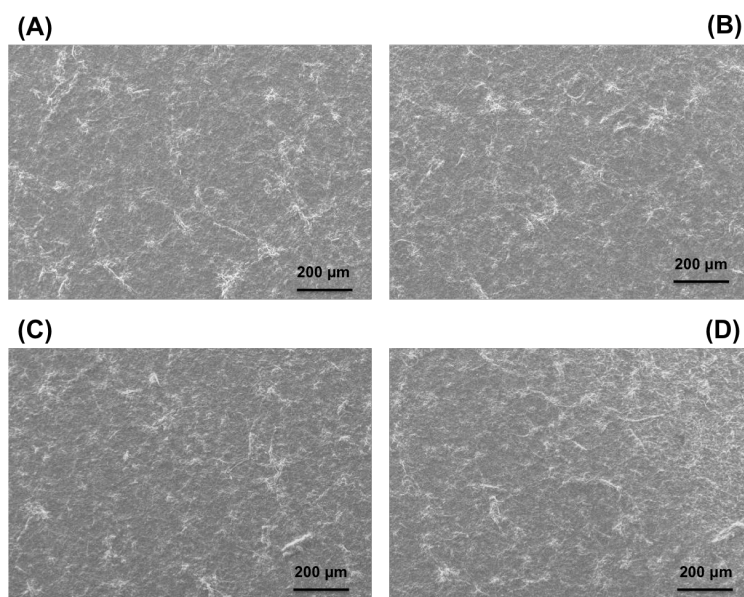


Figure S2: SEM images of fabricated membranes. SEM images of fabricated membranes were captured at 3 kV using low-resolution microscopy. SEM images of pristine-CMF, phosphorylated-CMF, carboxylic-CMF and methyl-CMF membranes were represented in image (a), (b), (c) and (d), respectively.

4.2. Surface ζ -potential measurement:

Mutek SZP 06, MUTEK (Sweden) device was used for the measurement of ζ -potential of suspensions (pristine-CMF, TEMPO-oxidized-CMF, phosphorylated-CMF and methyl-CMF). The ζ -potential of suspensions was measured respect to pH ranges (2 to 12) as shown in **Figure S3**. Furthermore, quantitative measurement of functional groups density is reported in **Table S1**.

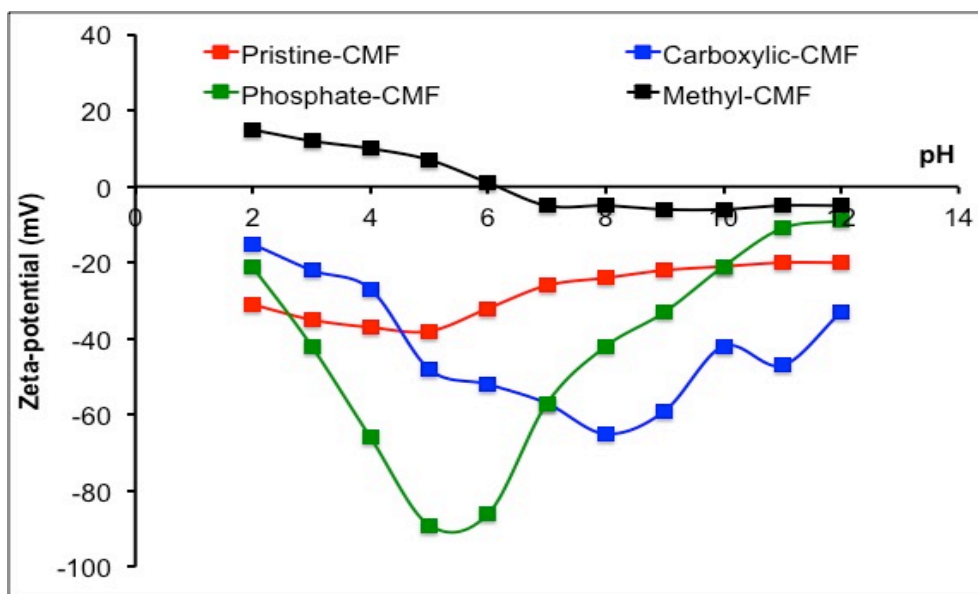


Figure S3: ζ -potential of pristine and functionalized CMF suspensions. 500 ml of suspension was used for the measurements. Reported data was in an average of three independent measurements.

4.3. Quantitative analysis of functional groups (functional group density):

4.3.1. Carboxylic: Conductometric titration was done with a three-necked round-bottom flask as discussed by Junka et al.⁴ In detail, the prescribed amount of CMF was diluted, 2 ml of 0.1M NaOH was added, and the dispersion was mixed for 1 h at 400 rpm at a total volume of 495 ml. after mixing, the ionic strength of the dispersion was adjusted with NaCl (5 ml of 10 mM NaCl) and samples were titrated with 0.1 M HCl using automatic titrator. CO₂ was removed by bubbling N₂ gas before and during titration. The total amount of functional groups in the sample was determined from the titration curve (conductivity as a function of the amount of H⁺ added)⁵.

4.3.2. Phosphate: Furthermore, the concentration of phosphate groups on CMF was determined using Inductive Coupled Plasma Atomic Emission Spectroscopy (ICP-OES, Optima 2000 DV, Perkin Elmer, USA) after the mineralization of native and phosphorylated-CMF samples in boiling HNO₃ and H₂O₂. In order to ensure the acidic form of phosphate groups, samples were first washed several times with diluted HCL to pH 4.0 and then mineralized⁶.

4.3.3. Methyl: The determination of methyl groups content was made through the method discussed by Chen⁷ with some modifications as discussed by Viera et al.³.

Table S1: Quantitative analysis of functional group density

Types of CMF	Charge density ($\mu\text{mole/g}$)
Pristine-CMF	28.54 \pm 4.1
Carboxylic-CMF	41.52 \pm 2.5
Phosphate-CMF	198 \pm 2.4
Methyl-CMF	12.21 \pm 3.1

4.4. Infrared spectroscopy: Varian 670- IR FTIR spectrometer was used for the measurement of all surface modifications and interaction within produced frameworks. The used spectrometer was equipped with an attenuated total reflection (ATR) detection device. All samples were scanned in the spectral region of 500-4000 cm^{-1} .

In order to determine the functionalization of cellulosic microfibers, the ATR-FTIR spectroscopy was performed as shown in **Figure S4**. Pristine-CMF has similar FTIR spectra as reported for cellulose nanofibers and cellulose nanocrystals^{8,9}, the broad band centered at ca 3500 cm^{-1} was related to O-H stretching vibration. The band at 3100 cm^{-1} and 1431 cm^{-1} were characteristic of C-H stretching and bending of CH_2 groups, respectively, where the peaks at 1160 cm^{-1} and 1070 cm^{-1} were typical to the saccharide structure as mentioned and summarized in our previous article⁸ for cellulose nanocrystals. Potentiometric titration was performed further to calculate the charge density of hydroxyl groups (**Table S1**) on pristine-CMF and it was to 28.54 \pm 4.1 $\mu\text{mole/g}$ ⁵.

The peak at 1605 cm^{-1} attributed to $-\text{COONa}$ due to the $\text{C}=\text{O}$ stretching of carboxyl groups¹⁰ in the spectra of TEMPO oxidized CMF based membranes. Furthermore, the effect of increased NaClO volume (3 to 10 ml) on functionalization was checked (**Figure S5**). The decrease peaks with respect to increase in the volume of NaClO was detected (**Figure S5**). The charge density of carboxylic group ($-\text{COO}$) was further calculated as reported in method section, decrease in charge density of carboxylic groups from 41.52 \pm 2.5 to 28.11 \pm 2.1 $\mu\text{mole/g}$ was detected as reported in **Table S2**.

The change in peak at 1210 cm^{-1} and 930 cm^{-1} assigned the phosphorylation of pristine-CMF which represents the $\text{P}=\text{O}$ and $\text{P}-\text{OH}$ vibration mode, respectively (**Figure S3**)^{2,11}. The increase in the absorbance of the peaks at 1645 cm^{-1} (i.e.

deformation vibration of water molecules) also suggests incorporation new hydroxyl groups by phosphorylation with increase water uptake. Effect of MgCl_2 concentration on the phosphorylation was detected using ATR-FTIR and potentiometric titration experiments. As shown in **Figure S4**, decrease in peak intensity with increased concentration of MgCl_2 (50 to 200 mM) was detected. In parallel, decrease in the carboxylic charge density was also recorded in titration experiment (**Table S2**). It has been presorted in the previous published article that high concentration of MgCl_2 inhibit the activity of hexokinase enzyme².

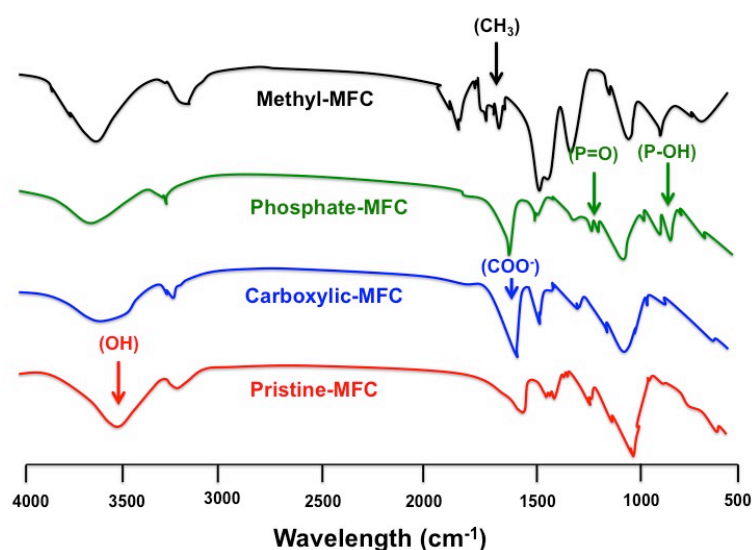


Figure S4: ATR-FTIR analysis of functionalized CMF based frameworks. Introduction of various functional groups were shown by multiple peaks

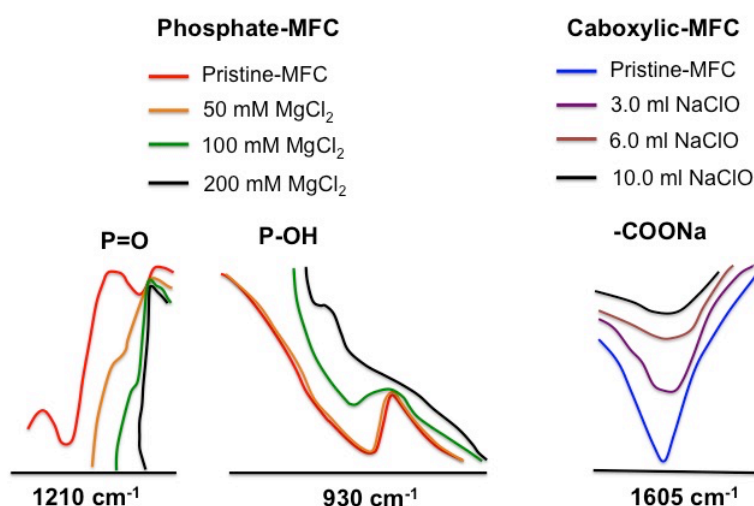


Figure S5: ATR-FTIR analysis of functionalized CMFs (phosphate-CMF and carboxylic-CMF). Change in the intensity by adding MgCl_2 (50-200 mM) has been shown here, with a high concentration of MgCl_2 , peaks at 1210 cm^{-1} and 930 cm^{-1}

vanished. In the case of carboxylic-MFC, peak at 1605 cm^{-1} is shown respect to the various volumes of NaClO. The intensity of peaks is decreased by increasing the concentration of NaClO.

Table S2: Quantitative analysis of functional group density of phosphate-CMF and carboxylic-CMF

Types of CMF	Variation in chemicals	Charge density ($\mu\text{mole/g}$)
Carboxylic-MFC	3.0 ml NaClO	41.52 ± 2.5
	6.0 ml NaClO	32.34 ± 1.6
	10.0 ml NaClO	28.11 ± 2.1
Phosphate-CMF	50 mM MgCl_2	198 ± 2.4
	100 mM MgCl_2	120 ± 4.2
	200 mM MgCl_2	80 ± 2.1

Methylation of microfibrillated cellulose was performed using chemicals. Main difference between pristine-CMF and methyl-CMF is the decrease in the intensity and change in the profile for the 3400 cm^{-1} band attributed to the stretching of the O-H bond (hydroxyl) due to partial substitution of hydrogen group during methylation of CMF. Furthermore, an increase is observed for the bands around 3200 cm^{-1} assigned to the C-H stretching due to the presence of the CH and CH_2 groups of cellulose and CH_3 of methyl-CMF. Methyl-CMF spectra usually present bands at 1460, 1380, 1320 and 950 cm^{-1} attributed to C-H stretching of CH_2 and CH_3 (**Figure S4**)¹². The change in the profile of the band assigned to the stretching of the bond O-H and the region assigned to stretch C-H confirms the efficiency of the methylation process.

4.5. ^{13}C CP MAS and ^{31}P MAS NMR spectroscopy:

The ^{13}C CP/MAS NMR spectra were recorded at $295 \pm 1\text{ K}$ in a Bruker Avance III AQS 400 SB instrument operating at 9.4 T for pristine and phosphate-CMF. The MAS rate was 10 kHz and a double air bearing probe and zirconium oxide rotor were used. Spectra were acquired with a CP pulse sequence using a $2.95\text{ }\mu\text{s}$ proton 90° pulse, a $800\text{ }\mu\text{s}$ contact pulse, and a 2.5 s delay between repetitions. Glycine was used for the Hartmann-Hahn procedure. The chemical shift was calibrated to the TMS

(CH₃)₄ Si scale by assigning the data point of maximum intensity in the α -glycine carbonyl signal to a shift of 176.03 ppm. For each sample, a total of 4096 or 16384 transients were recorded, resulting in an acquisition time of approximately 3 or 12 h, respectively².

The ³¹P MAS NMR spectra were recorded in a Bruker Avance instrument using a MAS rate of 10 kHz and a 4 mm probe as reported by Ghanadpour et al.¹³. Data were acquired using a contact time of 5 ms of a 90° pulse with a 10 s delay between repetitions. A total of 180 scans were recorded for each sample. The chemical shift values were referenced to 85% phosphoric acid (H₃PO₄).

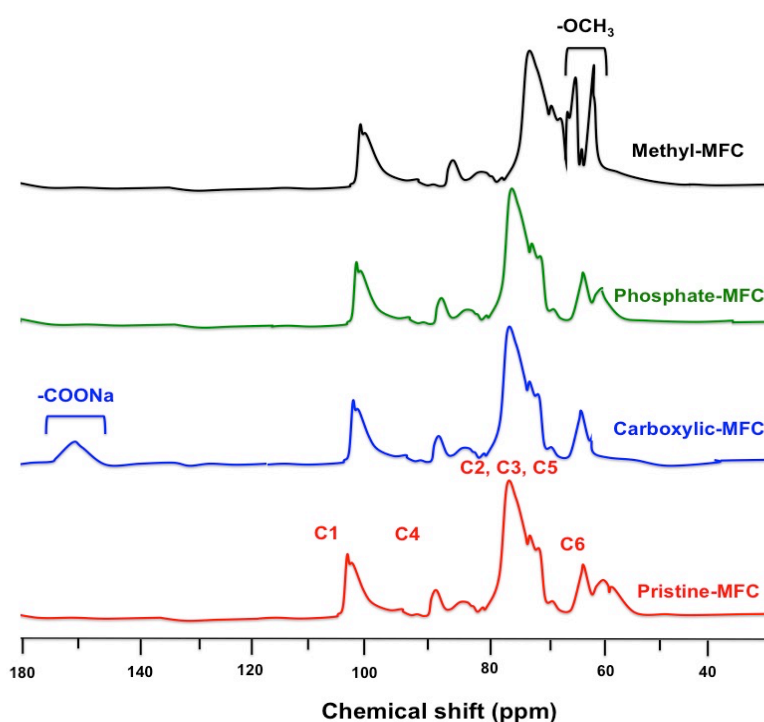


Figure S6: ¹³C CP/MAS NMR spectra of unmodified (pristine-CMF) and functionalized-CMF. All carbons (C1, C2, C3, C4, C5, and C6) have been reported in this ¹³C CP/MAS NMR spectra, and displacement after functionalization using various chemicals was also recorded.

The ¹³C CP/MAS NMR studies were carried out to elucidate the possible reaction mechanism and region-selectivity (**Figure S6**). For the original CMF, the typical signals of CMF appear at 107 ppm (C1), 76 and 73 (C2, C3 and C5) and 66.6 and 64.4 ppm (C6). A new peak at 176 ppm is ascribed to the sodium carboxylate carbons in the oxidized cellulose when compared to pristine-CMF. These results are consistent

with the previous relevant report¹⁴. Carboxylic-CMF had nearly no influences on the chemical shift and the pattern of C1 or C4 in solid state ^{13}C CP/MAS NMR. However, the oxidized CMF has large resonance peaks due to the original C6 primary alcohol groups of the glucose at about 67.3 ppm. Meanwhile, the signal at 64.4 ppm for C6 carbon sharply decreases and disappears when it is compared with the pristine-CMF, which indicates selective oxidation of the primary OH-units.

Furthermore, the influence of NaClO volume on functionalization was determined. **Figure S7** indicates the possible fluctuation in the observed peaks. Slight decrease in 176 ppm was observed after an increase in NaClO volume.

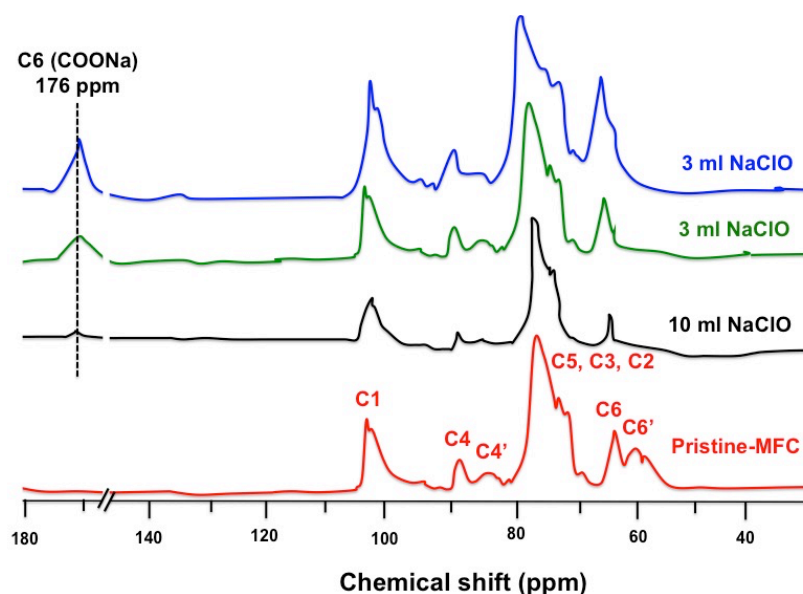


Figure S7: Effect of NaClO on carboxylation of CMF

As can be seen from the spectra (**Figure S7**), the noticeable signals within the region between 50 and 110 ppm can be defined as being mostly attributed to different carbons of cellulose: the region at 58-68 ppm is assigned to C6 (i.e. C6 is a crystalline and C6' is an amorphous cellulose). The cluster of signals at 68-80 ppm can be assigned to C2, C3 and C5, respectively; the region at 80-91 ppm assigned to C4 (i.e. C4 is crystalline and C4' is amorphous cellulose), and finally the region at 101-109 ppm can be assigned to C1. After both, the heterogeneous and homogeneous, the phosphorylation reactions' changes within the spectrums could be observed of position C4 and C6. By comparing the spectra of hexokinase-ATP treatment with increasing MgCl_2 concentrations results in more extensive structural changes and increase the spectral complexity of the pristine-CMF. The chemical shift observed for C6, which moved from 65.5 to 55.2 ppm after its substitution by the phosphate group.

By spectral de-convolution and fitting the C6 signal with three to five Lorentzian lines, it is possible to separate the integrated signal intensity assigned to crystalline cellulose from the total signal intensity of the C6 range.

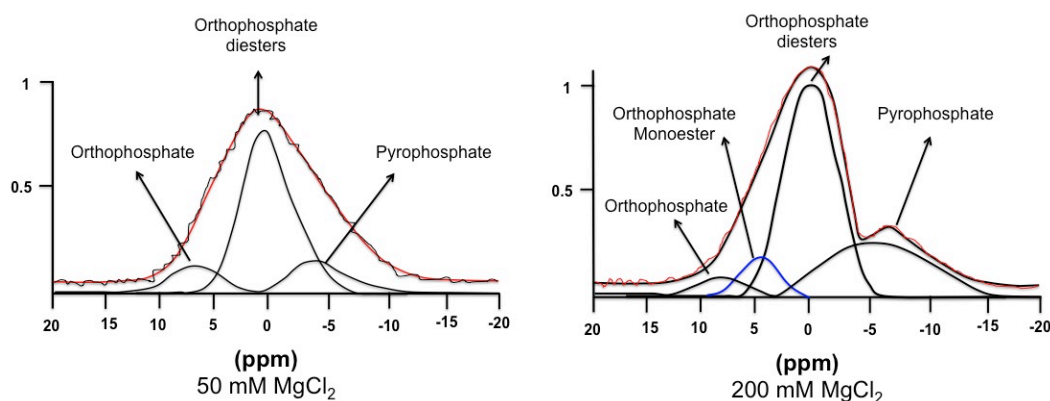


Figure S8: ^{31}P MAS NMR spectra of phosphorylated-CMF using 50 and 200 mM MgCl_2 at 50 mM ATP and 35 U/ml of hexokinase

Furthermore, when using 200 mM MgCl_2 , the highest DS value was obtained, and the chemical shift of C6 bearing OH groups available for substitution was shifted, and the amorphous spectral part split, thus confirming that phosphorylation only occurred at the C6 position.

The pristine-CMF did not show any peak (data not shown), whereas the spectrum of phosphate-CMF using 50 and 200 mM MgCl_2 showed clear peaks within the range of +15 to -15 ppm (**Figure S8**). This shift is typical for phosphoric mono- and diesters, and thus confirmed the presence of the phosphoric ester in CMF. The peaks of the solid-state spectrum are broad, each of which overlaps the chemical shifts of several P nuclei. However, peak identification and quantifications in the spectra can again be improved with their de-convolution resulting to three peaks, at samples being treated with 50 mM MgCl_2 , corresponding to the orthophosphate, orthophosphate diesters and pyrophosphate, respectively. Whereas in the case of using 200 mM MgCl_2 four peaks were identified, i.e. peaks at 7.0, 4.4, 1.8 and -6.3 ppm corresponding to the orthophosphate, orthophosphate monoester, orthophosphate diesters, and pyrophosphate, respectively¹⁵.

The methylated samples have four resonance lines divided into three different spectral ranges (105, 85/75 and 60 ppm), which can be distinguished in the ^{13}C NMR

spectrum. The C1 carbon signals for methyl-CMF samples appear in the same resonance line of cellulose at 105 ppm. Carbons C2, C3, C4 and C5 signals appear in the double peak region at 85 and 75 ppm. However, if C6 is substituted, these C6 resonances also fall into this spectral range. Finally, the signals of all unsubstituted C6 carbons and of all methyl groups, replaced in the methylation, compose the resonance line around at 60 ppm (**Figure S6**).

4.6. XRD analysis:

X-ray diffraction measurement was performed on a D/max III X-ray diffractometer (Rigaku Tokyo, Japan), equipped with nickel-filtered Cu K α radiation ($\lambda = 0.15418$). The diffraction angles (2θ) ranged from 5° to 40° , and the step size was 0.04° . A Lorentzian deconvolution was used for peak separations. The d -spacing (d) of the produced nanolaminate membranes were calculated with the Bragg equation¹⁶

$$d = \lambda / 2 \sin \theta \dots \dots \dots \text{Eq (1)}$$

Where λ is the wavelength of X-ray source (0.15418) and θ is the Bragg angle corresponding to the plane.

Table S3: lamellar structure of functionalized CMF membranes

MFC Sample	Interlayer Spacing d (Å)	Bond Length (Å)
Pristine	4.44	O-H = 0.97
Carboxylate	5.36	C=O-O = 1.20-1.34
Phosphorylated	11.44	P=O = 1.56
Methylated	6.86	C-H = 1.09

The interlayer spacing of the fabricated laminated membranes was calculated using d spacing as discussed above and the obtained results were reported in **Table S3**. **Table S3** further demonstrate the increase in the d spacing after functionalization of CMF laminated membranes, which was further supported by various other experimental analysis like water permeation, BET pore-size distribution and Molecular Weight

Cut-Off experiments. Theoretical dimensions of grafted functional groups are 0.97 Å, 1.43 Å, 2.18 Å and 4.47 Å for hydroxyl-, carboxylic-, methyl- and phosphate-, respectively, which clearly indicates the increase in interlayer spacing after introduction of these functional groups.

XRD spectrum of all laminated membranes was also measured in wet state as reported in **Figure S9**. All laminated membranes were analysed after 48 h dipping in water.

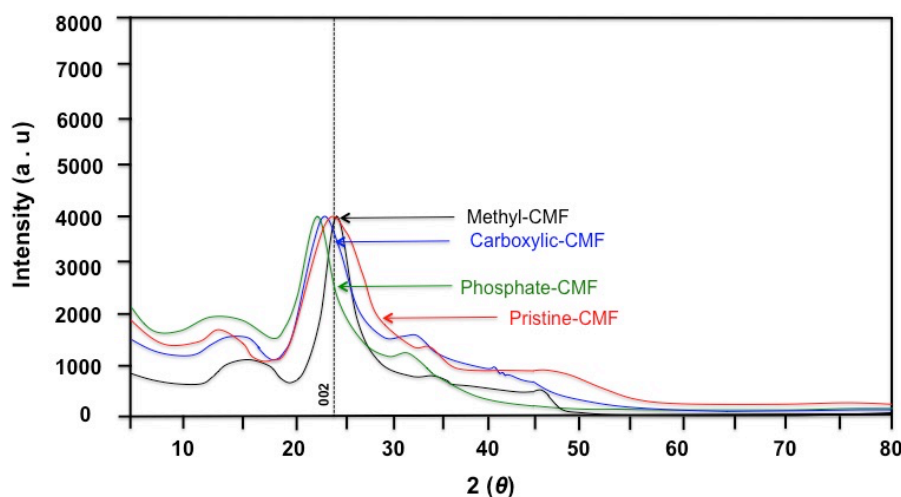


Figure S9: Full XRD spectrum of wet membranes after 48 h of incubation in water

In **Figure S9**, decrease in intensity of wet laminated membranes was recorded and the shift of (002) peak compared to pristine-CMF was also observed. The right shift of (002) peak of methyl-CMF laminated membranes indicates the shrinking of laminated membranes after incubation in water. In our opinion, some detailed study is needed to understand the effect of moisture on *d* spacing in depth and it might be the future study in our lab.

4.7. XPS analysis of functionalized CMF:

The X-Ray photoelectron spectroscopy analyses were carried out on the PHI-TFAXPS spectrometer produced by Physical Electronics Inc. The analyzed area was 0.4 mm in diameter, and the analyzed depth was about 3-6 nm. The sample surfaces were excited by X-ray radiation from a monochromatic Al source at a photon energy of 1486.6 eV. The high-energy resolution spectra were acquired using an energy analyzer operating at a resolution of about 0.65 eV and pass-energy of 187 eV. During data processing the spectra from the surface were aligned by setting the C–C/C–H peak in the C 1s spectrum to a binding energy of 285.0 eV. The accuracy of

the binding energy was about ± 0.3 eV. The concentrations were calculated from the intensities of the peaks within the XPS spectra using relative sensitivity factors provided by the instrument's manufacturer. Two spots were analyzed on each sample, and the average composition was calculated.

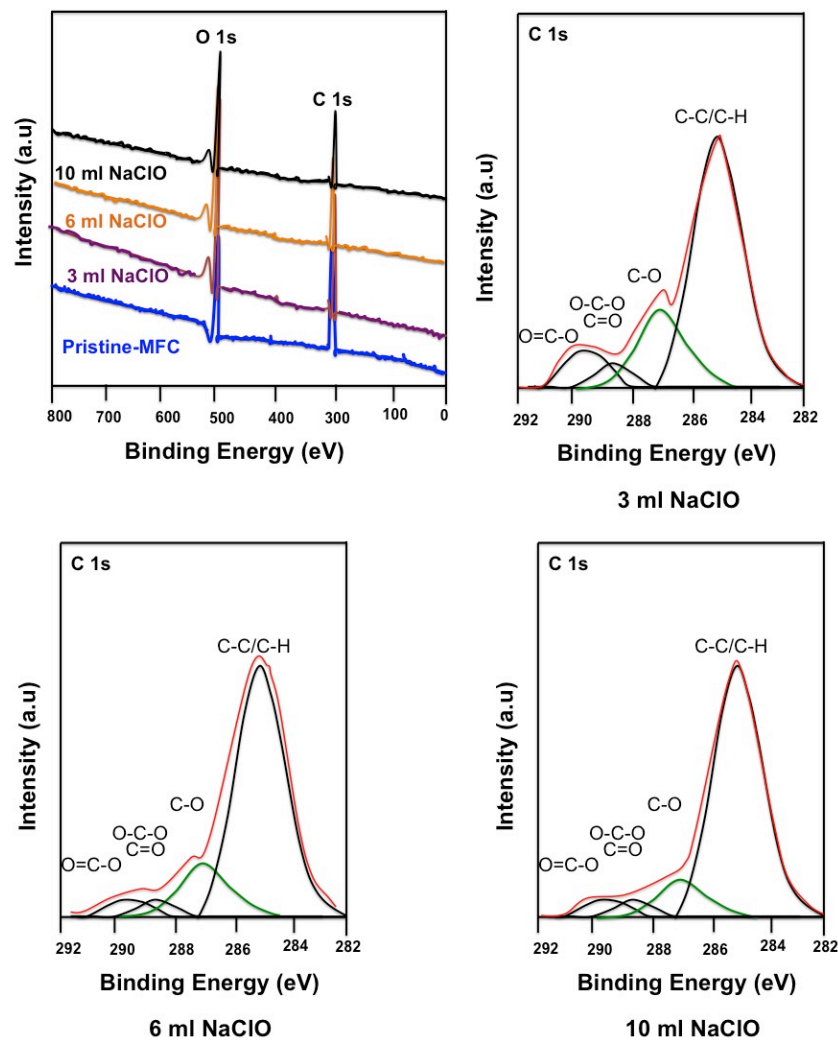


Figure S10: (A), Survey XPS core level spectrum of pristine and carboxylated-CMF using different concentration of NaClO

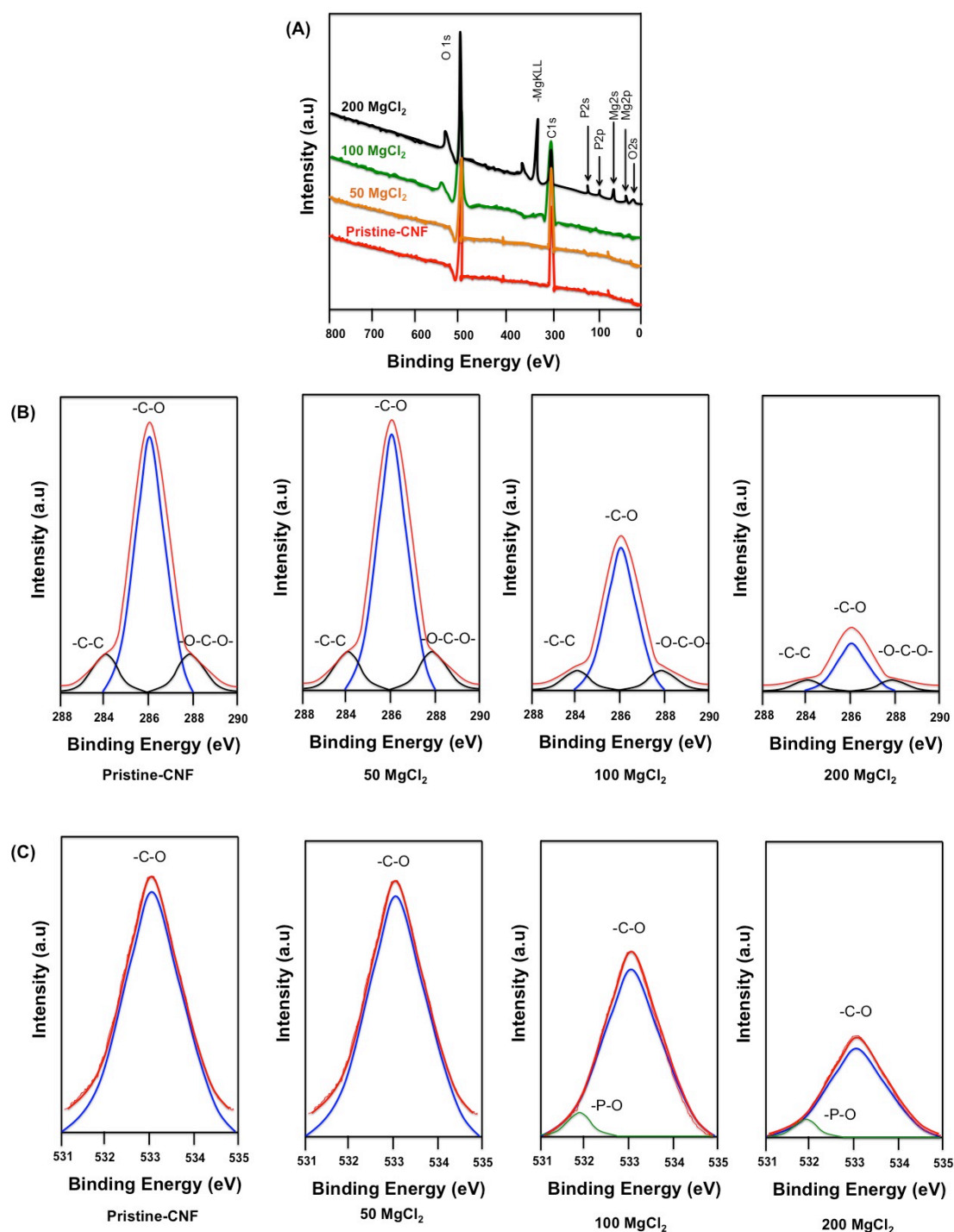


Figure S11: (A), Survey XPS core level spectrum of pristine and phosphorylated-CMF using different concentrations of MgCl_2 . (B), High-resolution scans of C 1s of native and modified-MFC. (C), High-resolution scans of O 1s of native and modified-CMF.

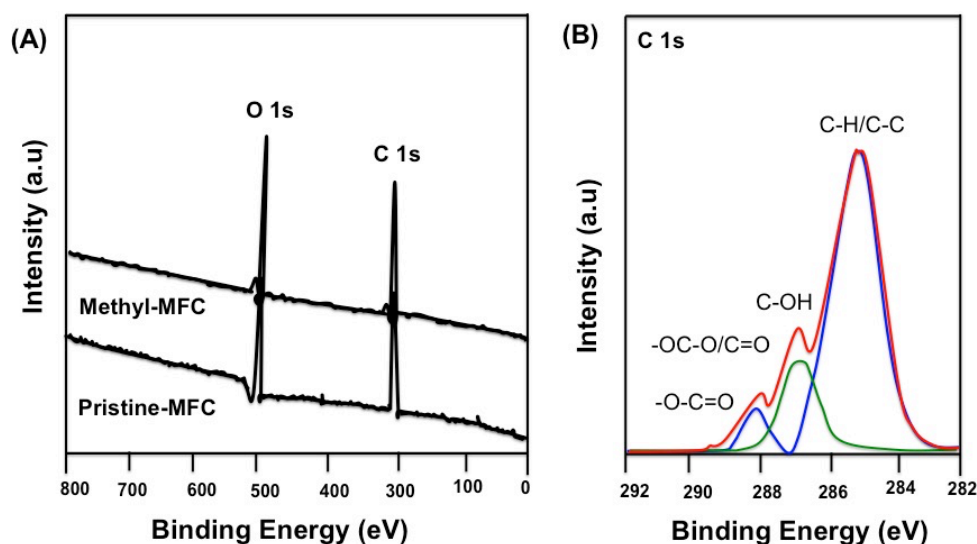


Figure S12: Methylation of CMF. (A), Survey XPS core level spectrum of pristine and methylated-CMF and (B), high-resolution scans of C1s of native and modified-CMF (methylated)

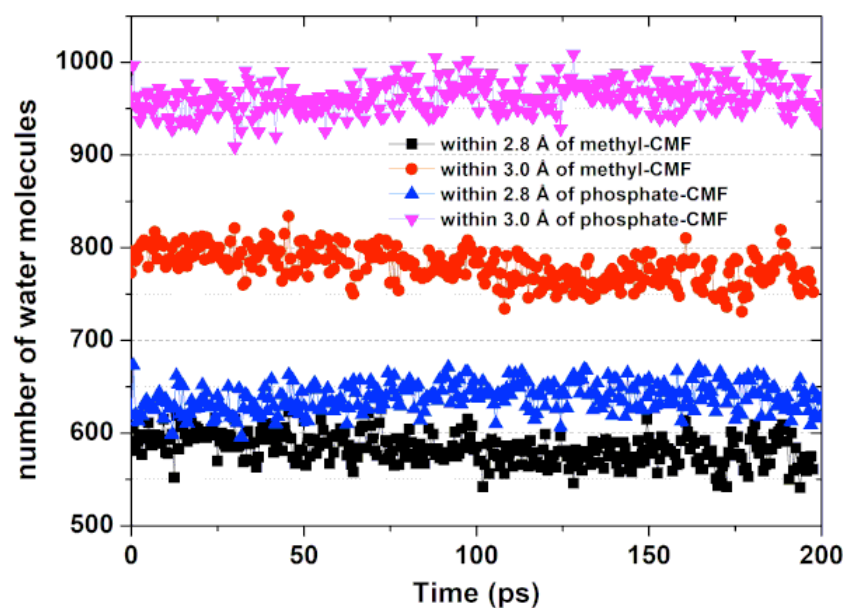


Figure S13: Computational simulations of the solvation effect on methylated and phosphorylated CMF (when they are not dried but evolving in solution). Here we can see the trend of the water content (number of water molecules within 2.8 and 3.0 Å of the fibers) during the last portion of the dynamics (and the distribution)

When the chains of phosphate-CMF are extended their length is comparable to that of the methyl groups (practically, we have a broad distribution of chain lengths) but the degree of bending depends on the interactions of the various headgroups with the groups close by (these could belong to other fibers as well).

The interlayer spacing is determined by the type and strength of these interactions. In the case of methyl groups, they seem more repulsive than in the other case (especially when the methyl moieties are face-to-face). We should also consider the fact that methyl groups are more hydrophobic than phosphate groups (that are neutralized by counterions and solvated by water). The adsorbed waters (just a few molecules) play a sort of gluing effect between the fibers. These waters are almost absent in the case of methylated cellulose. Therefore, a greater separation between the fibers when we insert methyl groups seems more probable.

Furthermore, the *size* of the phosphate groups is larger than the one of the methyl groups. This could explain the tendency towards broader interlayer separations in the phosphate-CMF membranes. In **Figure S13** orange regions in methyl-CMF membranes indicate more open structures (i.e. a wider intercapilar spacing) compared to phosphate-CMF membranes.

4.8. Water permeability:

Water permeability of all produced frameworks was calculated using Convergence Clean Water Flux (CWF) pilot system as shown in **Figure S14**. All produced frameworks were fixed in the module (size: 7 x 11 cm). First, membranes were fixed in the module, and all air bubbles were taking out by supplying water at low pressure (0.5 bar). The permeate flow rate was monitored using a high precision balance. Water permeance of frameworks was recorded at defined pressure after reaching the equilibrium and reported as $\text{Lh}^{-1} \text{m}^{-2}$.

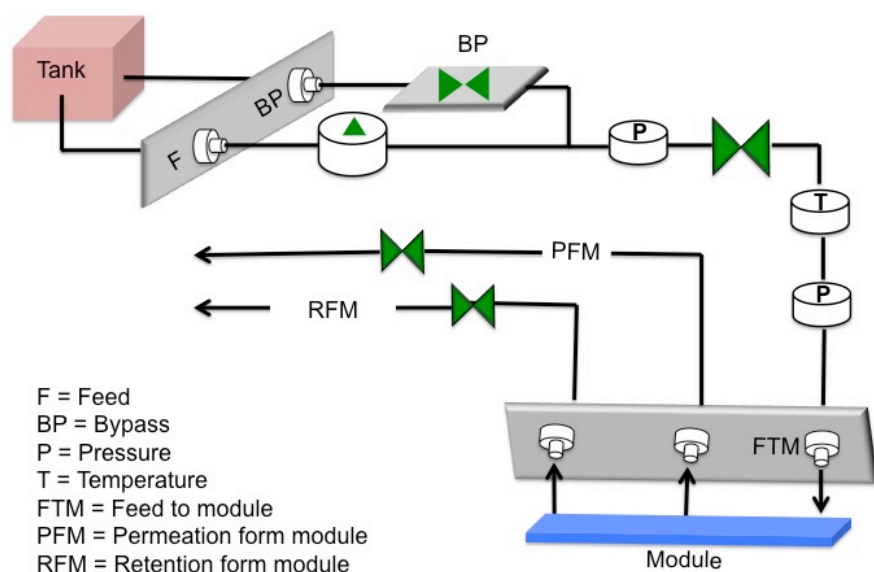


Figure S14: Convergence Clean Water Flux (CWF) pilot system was used for the measurement of water flux through the produced dimensional frameworks. Water flux was measured in continuous mode at a defined pressure. Membrane area used for measurement was $\approx 77 \text{ cm}^2$.

The highest water flux was recorded for the phosphate-CMF membrane, where the interlayer spacing was broader compared to other fabricated nanolaminate membranes. Considering that the grammage of the produced membranes is also essential for an efficient filtering process, it was interesting to disclose the effect of grammage on the water flux. An increase in the grammage of membranes determined a decrease in the water flux in all cases. The highest water flux was recorded for the phosphorylated-CMF membranes with a 50 g/m^2 grammage (**Figure 2C**).

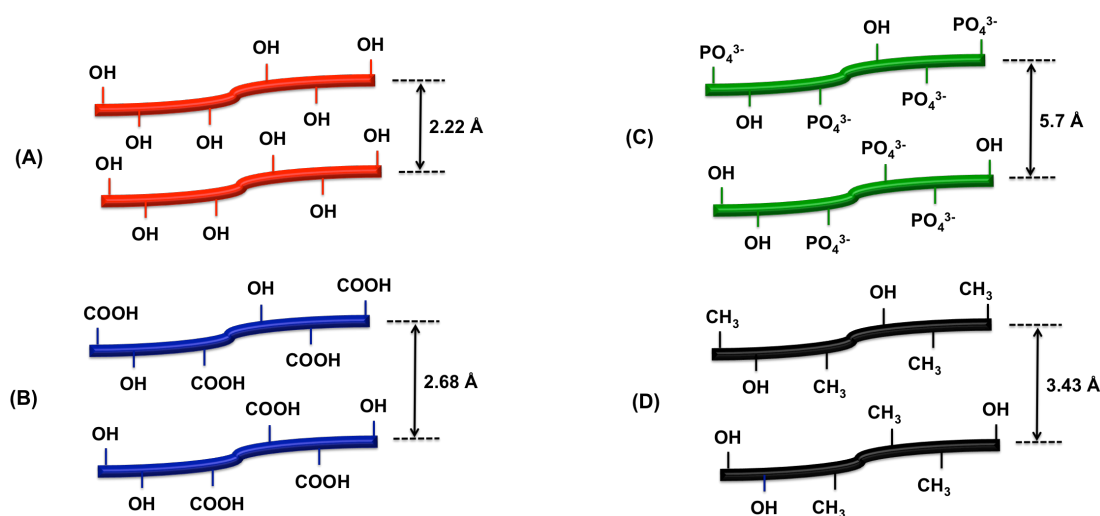


Figure S15: The increase in the inter-fiber spacing after the functionalization of CMF. **(A)**, Pristine-CMF has hydroxyl functional groups on the CMF surface. **(B)**, after TEMPO functionalization, carboxylic groups were introduced, thus, an increase in the inter-fiber spacing was observed according to the diameter of COOH groups. **(C)**, Highest inter-fiber spacing was obtained for phosphate functionalized CMF. **(D)**, Nonpolar attachment of methyl groups also increases the inter-fiber spacing between the fibers.

4.9. Molecular weight cut-off (MWCO):

The molecular weight cut-off of fabricated membranes was performed using solute of polyethylene glycol (PEG) of different molecular weight from 1 to 50 kDa. The rejection as a function of PEG standards is shown for all laminated membranes in **Figure S16**. The MWCO is defined as the molecular weight of which 90% of solute is rejected. From **Figure S16** it can be easily seen that high MWCO was detected for all laminated membranes and lowest MWCO was observed for pristine-CMF laminated membranes (≈ 3 kDa), it is not surprising that all membranes have low MWCO values. Phosphate-CMF membranes have highest MWCO value (≈ 11 kDa) as reported in **Figure S16**. According to the Mautner et al.¹⁷ (2015), 25 kDa molecular weight is equal to 5 nm hydrodynamic radius of PEG, therefore all fabricated laminated membranes have lower than 5 nm of pore diameters.

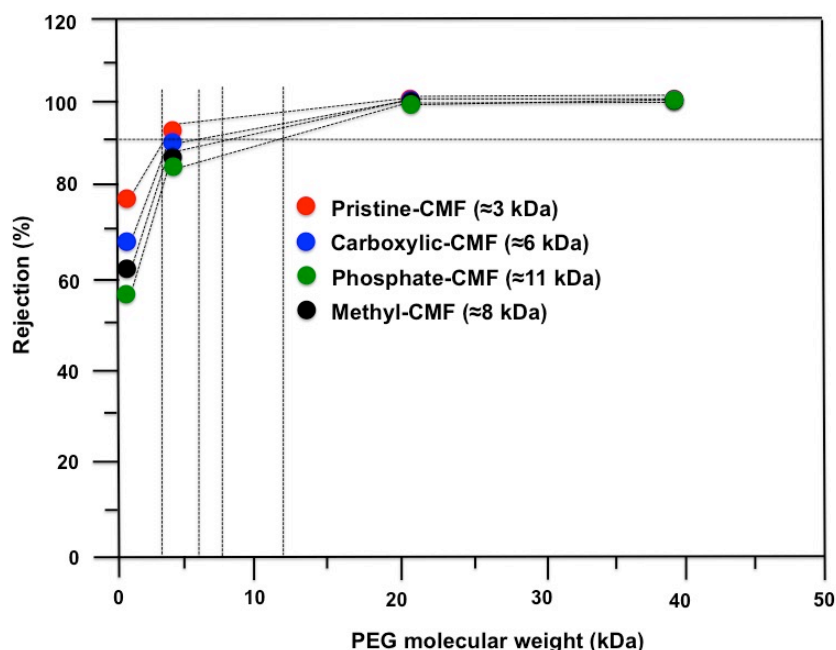


Figure S16: MWCO of all laminated membranes was performed using PEG solution as described by Matner et al.¹⁷ (2015).

4.10. BET measurement: Pore-size distribution and average pore size of nanolaminate composite membranes were measured using a Micromeritics ASAP 2000 instrument, and the samples were degassed at 100°C for 24h in dry N₂ flow prior to measurements. First, all produced membranes were cut into small pieces and > 2 g of each sample was used for measurement. The detailed explanation is discussed by Karim et al.⁸.

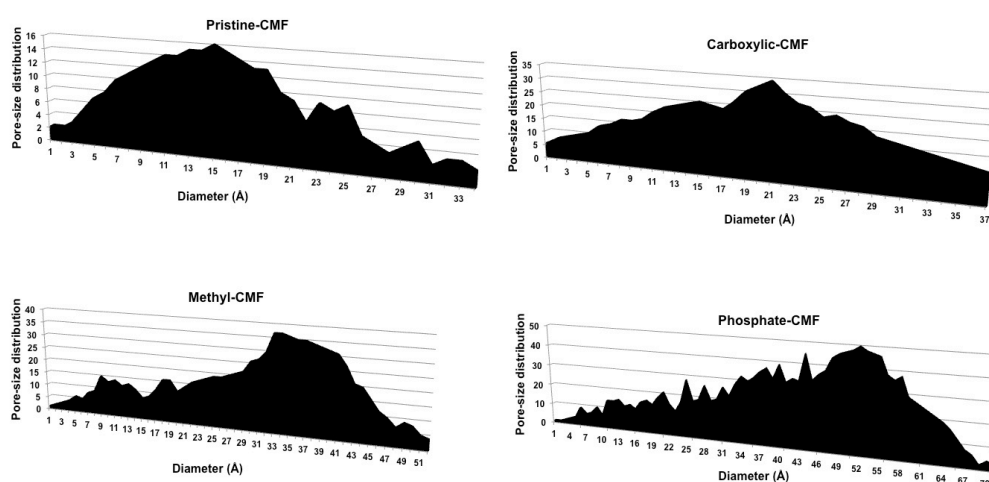


Figure S17: BET pore-size distribution of fabricated laminated membranes. BET was performed to analyzed the pore-size distrintion as reported by karim et al.⁸. Increate in pore-size distribution was recorded after functionalization of CMF membranes compared to pristine-MFC.

Obtained BET results are reported in **Figure S17** and it is very clear that increase in pore-size diameters was observed afted functionalization of CMF (supported by water flux studies too). Pore-size distribution as function of pore volumn was close to 15 Å for pristine-CMF membranes which is further supported by MWCO analysis (≈ 1.2 nm). Increase in pore-size distribution after functionalization was in the order of phosphate-CMF > methyl-CMF > carbolylic-CMF > pristine-CMF and increase in interlayer space of laminated membranes was also recorded in the same order.

Table S4: BET analysis of fabricated nanolaminated composite membranes

Membranes	Functional groups	BJH adsorption pore width (Å)	BJH desorption pore width (Å)
Pristine-CMF	-OH	15	17
Carboxylic-CMF	-COOH	30	32
methyle-CMF	-CH ₃	35	42
Phosphate-CMF	PO ₄ ³⁻	50	56

4.11. Mechanical properties and Air permeance: The tensile strength of all produced frameworks was measured using a tensile tester (Lorentzen & Wettre, ABB, Sweden), as discussed in our recently published article.

Air permeance of samples was measured using L&W air permeance tester (Lorentzen & Wettre, ABB, Sweden). First, calibration of the tester was performed, and then samples were placed under holder and defined air pressure was applied.

Table S5: All produced frameworks were tested in tensile mode and air permeance was calculated as shown above

Types of structures	Max stress (MPa)	Strain at break (%)	Modulus of Elasticity (MPa)	Air permeance (µm/Pa,s)
Pristine-MFC	38±2.7	3±0.4	22±1.2	2.4±1.1
Carboxylic-MFC	35±2.1	2±0.3	24±3.1	3.1±2.1
Phosphate-MFC	32±1.3	2±0.2	26±2.2	4.5±1.5
Methyl-MFC	34±4.5	3±0.3	21±3.7	4.1±2.9

5. Nanolaminated membranes performance:

5.1. Ions permeation rate:

We performed the measurements for different ionic strengths corresponding to the salt concentration of 0.5 M, 0.10 M, and 1.5 M in the feed side system (Dead-End-Cell system with low applied pressure). The 1 M of NaCl was selected for NaCl rejection experiment. The applied vacuum was 0.5 bar. The percentage removal was calculated using equation given below

$$\text{Percentage removal} = \frac{C_f - C_p}{C_f} \times 100 \dots \dots \dots (i)$$

Where C_f is the concentration of feed, C_p is the concentration of permeate used in the measurements.

5.2. Membrane performance for removal of metal ions, dye, and drugs

The polluted water contaminated with metal ions was collected from an industrial site in Örnköldsvik, Sweden. The concentration of metal ions in the contaminated water is given in **Table S6** and pH of polluted water was acidic (5.4). **Table S6** further demonstrates the percentage removal and capacity of used nanolaminate membranes.

Table S6: Treatment of wastewater using functionalized nanolaminate composite membranes

Functionalized membranes	Removal (%)				Removal capacity (mg/g)			
	C _o (μg/L)							
	Mg ²⁺ (5800)	Cd ²⁺ (5.77)	Co ²⁺ (1.03)	Cr ³⁺ (9.87)	Mg ²⁺ (5800)	Cd ²⁺ (5.77)	Co ²⁺ (1.03)	Cr ³⁺ (9.87)
Pristine-MFC	7	39	26	30	165	250	198	221
Carboxylic-MFC	55	60	39	38	254	369	250	290
Methyl-MFC	48	27	34	20	244	200	188	190
Phos-MFC	67	81	75	80	364	544	370	454

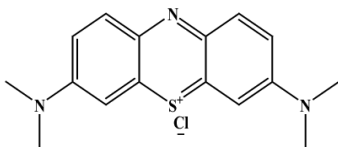
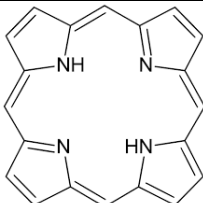
All metal ions were removed in cross-direction flow using Dead-End-Cell apparatus as discussed in our previous published article⁴. The known amount of polluted water

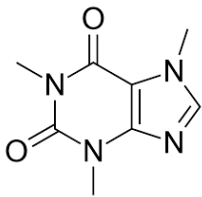
is filled in Dead-End-Cell column (300 ml) and passed through the used functionalized nanolaminate membranes. Percentage removal was calculated using equation (i). Capacity of used functionalized membranes was also calculated as mentioned below.

$$\text{Co-Ci} \times \text{V/W} \dots\dots\dots(\text{ii})$$

Where Co and Ci are initial and remaining concentrations of metal ions in mg/L^{-1} and V is the volume in liters and W is weight in grams of composite mmebranes.

Table S7: Contaminants details used for removal studies

Contaminants	Metal ions (µg/L)			Ref.
	Structure	Molecular weight (g/mole ⁻¹)	Stock radius (Å)	
Mg ²⁺ (5800)	Nil	24.305	0.86	Karim et al. ¹⁸
Cd ²⁺ (5.77)	Nil	112.4	0.95	
Co ²⁺ (1.03)	Nil	58.9	0.88	
Cr ³⁺ (9.87)	Nil	51.9	0.75	
Molecular dye				
Methyl blue		799,8	12.5	Karim et al. ⁸
Drugs				
Porphyrin		310.3	270	Ribeiro et al. ¹⁹

Caffeine		194.2	3.87	Price et al. ²⁰
----------	---	-------	------	----------------------------

Dye concentration of 15 mg/L was prepared in pH 5.0 in stock. The selected concentration was the highest limit in an industrial effluent, as discussed with the paper and pulp industry. Treatment experiments were performed in static as well as in dynamic mode. In static mode, nanolaminate composite membranes were incubated with model polluted water for 24 h (saturation limit), and then percentage adsorption was calculated by applying equation (i). Rejection percentage of dye was calculated in dynamic mode. The experiment was performed as discussed for the metal ions removal section. The high percentage rejection of composite membranes in dynamic mode might be due to a large number of functional groups available for the immobilization of molecules dye.

The effect of pH on the removal of molecular dye was observed, and the obtained results are reported in **Figure S18**. It has been found that obtained zeta-potential of produced nanolaminate membranes have a direct influence on the adsorption of molecular dye. An increase in adsorption percentage was recorded with a decrease in zeta-potential of fabricated membranes (**Figure S3**).

Concentrations of drugs used for the rejection study were 1 M. Both drugs were dissolved in a buffer solution having pH 5.0, and all rejection experiments were performed in dynamic modes as discussed in the case of metal ions and molecular dye rejection studies. The percentage of rejection was calculated by applying equation number (ii).

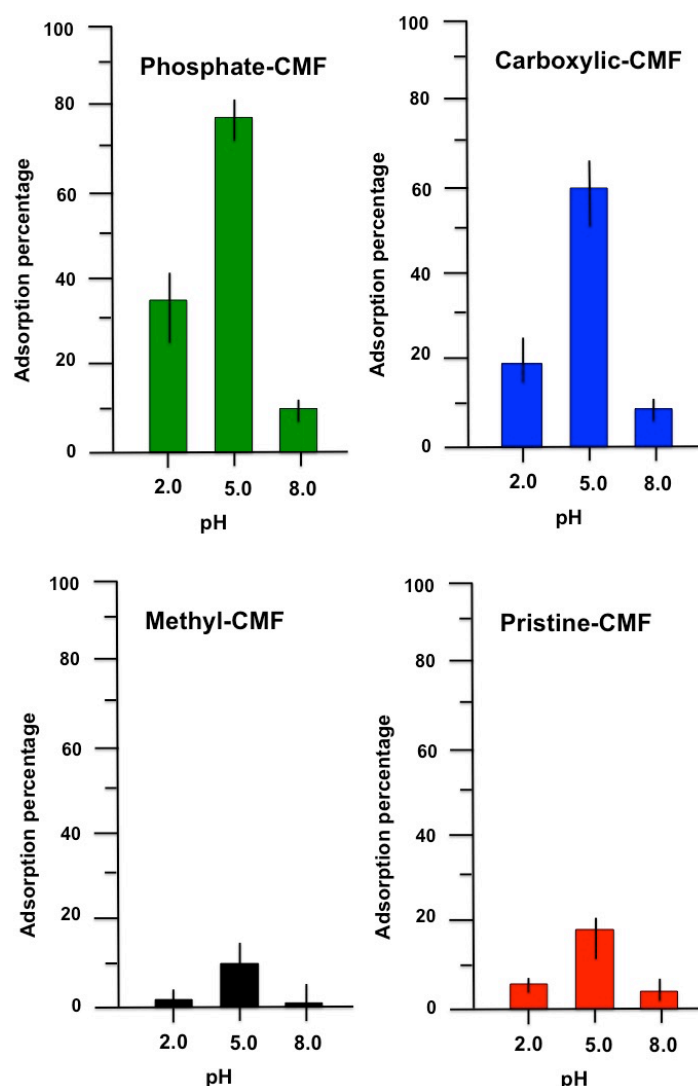


Figure S18: The effect of pH on the adsorption of dye was analyzed. Highest removal was observed for phosphate-CMF followed by carboxylic-CMF, pristine-CMF, and methyl-CMF.

5.3. Mechanical stability and removal of dyes in countinuous flow (Long Term Stability Analaysis):

Only two laminated membarnes (phosphate- and methyl-MFC) were used to understand the long term stability in countinuous flow using Convergence Clean Water Flux (CWF) pilot system as shown in **Figure S14**. All produced membranes were fixed in the module (size: 7 x 11 cm). First, membranes were fixed in the module, and all air bubbles were taking out by supplying water at low pressure (0.5 bar). After that water permeability was measured after 48 h and then laminated membarnes were taken out and tensile strength was measured as reported in previous section (**Section 4.11**).

To measure the saturation limit, laminated membranes were operated in continuous flow, stock dye solution of 15 mg/L (pH 5.0) passed through laminated membranes for 48 h. All parameters were same as discussed related to dye adsorption experiments in cross-flow mode. **Table S8** below illustrates the long term stability and saturation limit of used laminated membranes.

Table S8: Long term stability and saturation limit of laminated membranes

Membranes	Water flux after 48 h ($\text{Lh}^{-1}\text{m}^{-2}\text{bar}^{-1}$)	Max stress (MPa) after 48 h	Dye removal (%)	
			24 h	48 h
Phos-MFC	56±4.8	17±2.6	100	100
Methyl-MFC	29±1.8	14±1.9	100	100

In **Table S8**, it is clear that membranes are stable in continuous operation and no significant change and defects in visual morphology was recorded. Furthermore, complete removal of dye solution was recorded, indicate used membranes are still not reached to saturation limit. To find the saturation limit, 20 mg/L dye stock solution was prepared and the experiment was performed second time, approx. 86% removal of dye solution was calculated after 12 h of continuous flow, no significant increase in the percentage removal was calculated further.

6. Comparative study with literature:

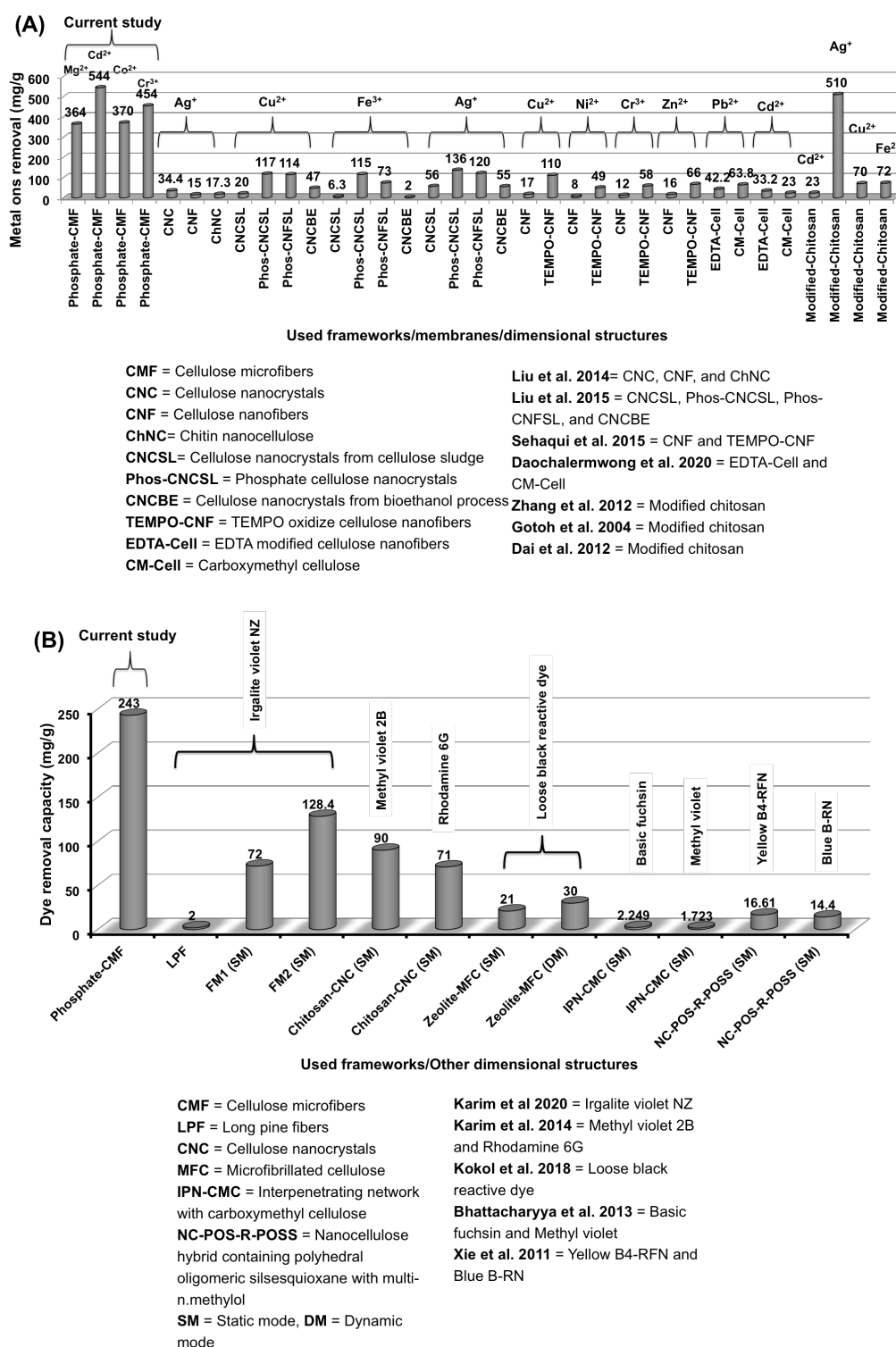


Figure S19: A comparative study of metal ions (A) and dyes (B) was performed with literature. High removal efficiencies (mg/g) were calculated for metal ions and dyes. In this image only phosphate-CMF was compared. It has also been observed that modified chitosan showed high removal capacity of silver ions compared to current

study. In image (B), FM represents frameworks/ dimensional structures. Ref. from 21 to 31.

7. Model Building and Simulation Details:

The nanocellulose (CMF) model is made of sixteen chains, which contain sixteen glucosyl residues each. They were shaped as a parallelepiped rod (approximately $84 \times 26 \times 26 \text{ \AA}^3$) and modified according to the experimental conditions, by replacing the $-\text{CH}_2\text{OH}$ groups exposed to the solvent with carboxyl (carboxylate-CMF), phosphate (phosphorylate-CMF) and methyl (methylate-CMF) moieties. The percentage of functionalized groups was based on experimental data. The resulting negatively charged systems were then neutralized by adding positively charged counterions (Na^+ and Ca^{2+}) and solvated by surrounding them with approximately 15000 water molecules (simulation box size: $84 \times 101 \times 54 \text{ \AA}^3$). The initial configurations were equilibrated, preliminarily, in the NPT ensemble at $T=300\text{K}$ for about 200 ps. Periodic boundary conditions were applied in all directions in such a way that the replication along x emulated a continuous infinite nanofiber.

The size of the system was appropriate to generate a reasonable variety of geometries with the different functionalizations useful for explaining and predicting the results of the experiments.

A preliminary simulation, approximately 500 ps long, was employed to generate a few different starting structures, which were then used to extend the sampling in each case. The total simulation time, which was around 5 ns, was sufficient to obtain relatively stable arrangements. The final analysis was focused on the last portions of the trajectories.

During the equilibration stage, carried out in the NPT ensemble at $T=300\text{K}$, constraints were applied to the solute and to the x dimension of the box to guarantee continuity, then the constraints were removed, and the simulations were extended saving the structure every 0.4 ps. The temperature was controlled through Berendsen's thermostat³² with a relaxation constant of 0.1 ps, and the time step was set to 0.5 fs. All reactive molecular dynamics runs were based on a previous parametrized force field tuned for these systems³³ and carried out with the ReaxFF code available in the Amsterdam Density Functional (ADF)/ReaxFF package [E. J.

Baerends et al. ADF, adf2014.05³⁴ installed on local clusters and workstations (at CNR-ICCOM/IPCF). The primary sampling was obtained through the LAMMPS package available at the CINECA supercomputing center (high-performance computing resources - ISCRA initiative).

The analysis of the last portion of the production trajectories was focused on the comparison of the three different models. The reorganization of the CMF chains was accomplished by checking the root mean squared deviations of the atoms relative to the average structure (calculated from the last hundred-picoseconds of the productions). The relative positions of the metal ions were examined in detail together with hydrogen bonds, protonation states, and solvation effects. Visual inspection of the trajectories was also useful to disclose the orientations of the functionalizing moieties and their elongation into the solvent.

To evaluate the packing capability of CMF, due to the different functionalizations, the final average configurations were dried by a two-step procedure. First, all the water molecules far from the CMF interface were removed, and the system was compressed, then it was equilibrated in the NPT ensemble at $T=300\text{K}$. Second, only those water molecules within 2.5 \AA of the CMF chains were retained, and the system was equilibrated again through a protocol similar to the first one.

It is worth mentioning that, due to the amorphous nature of the nanocellulose material in these complex environments and to the significant number of degrees of freedom, it is impossible, also by extending the number of models and the simulation times, to obtain fully detailed molecular models or more realistic representations of these supramolecular arrangements. Experimental characterization at the atomic level is likewise impossible, and only theoretical models can provide such descriptions deducing possible explanations of many of the effects observed experimentally. Although the complex aggregation and full stabilization of the CMF chains, water, ion, and counterions are very slow processes that cannot be fully disclosed with modeling (due to the extremely long simulation times - with the ion motion as the rate-determining step in the total convergence), the present simulations can provide explanations and ideas of the tendencies and trends of both the nanocellulose chains and the surrounding environment.

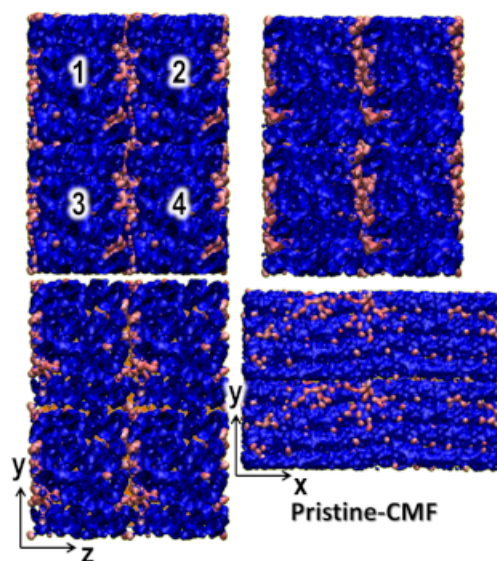


Figure S20. Packing of the dried fibrils models. The CMF fibers are rendered through the solvent-accessible surface, whereas water, channels, and cavities are displayed as orange areas. The numbers 1, 2, 3, 4 represent the replicated models, whereas the axes indicate the directions of the replication.

8. References

1. A. Serra, I. Gonzalez, H. Oliver-Ortega, O., Tarres, M. Delgado-Aguilar, P. Mutje, Reducing the amount of catalyst in TEMPO-oxidized cellulose nanofibers: Effect on properties and cost. *Polymer*, 2017, 9, 557-571.
2. M. Bozic, P. Liu, A. P. Mathew, V. Kokol, Enzymatic phosphorylation of cellulose nanofibers to new highly-ions adsorbing, flame-retardant and hydroxyapatite-growth induced natural nanoparticles. *Cellulose*, 2014, 21, 2713-2726.
3. R. G. P. Viera, G. Rodrigues Filho, R. M. N. de Assuncao, C. S. Meireles, J. G. Vieira, G. S. de Oliveira, Synthesis and characterization of methylcellulose from sygar cane bagasse cellulose. *Carbohydr. Polym.*, 2007, 67, 182-187.
4. K. Junka, I. Filpponen, T. Lindstrom, J., Laine, Titrimetric methods for the determination of surface and total charge of functionalized nanofibrillated/microfibrillated cellulose (NFC/MFC). *Cellulose*, 2013, 13, 2887-2895.

5. Z. Karim, A. Svedberg, K. Y. Lee, M. J. Khan, Processing-structure-property correlation understanding of microfibrillated cellulose based dimensional structures for ferric ions removal. *Sci. Rep.*, 2019, 9, 10277.
6. T. L. Ogeda, I. B. Silva, L. C. Fidale, A. O. El-Seoud, D. F. S. Petri, Effect of cellulose physical characteristics, especially the water sorption value, on the efficiency of its hydrolysis catalyzed by free or immobilized cellulose. *J. Biotechnol.*, 2012, 157, 246-252.
7. C. L. Chen, Methods in lignin chemistry. Berlin: Springer-Verlag, PP. 465-471 (1992).
8. Z. Karim, A. P. Mathew, M. Grahn, J. Mouzon, K. Oksman, Nanoporous membranes with cellulose nanocrystals as functional entity in chitosan: removal of dyes from water. *Carbohydr. Poly.*, 2014, 112, 668-676.
9. Z. Karim, M. Hakalahti, T. Tammelin, A. P. Mathew, A. P., Oksman, K. *In situ* TEMPO surface functionalization of nanocellulose membranes for enhanced adsorption of metal ions from aqueous medium. *RSC Adv.*, 2017, 7, 5232-5241.
10. A. Isogai, T. Hänninen, S. Fujisawa, T. Saito, Review: catalytic oxidation of cellulose with nitroxyl radicals under aqueous conditions. *Progress poly. Sci.*, 2018, 86, 122-148.
11. D. M. Suflet, G. C. Chittanu, V. I. Popa, Phosphorylation of polysaccharides: new results on synthesis and characterization of phosphorylation cellulose. *Teact. Funct. Polym.*, 2006, 66, 1240-1249.
12. R. L. Oliveira, J. G. Vieira H. S. Barud R. M. N. Assuncao, G. R. Filho, S. J. L. Ribeiro, Y. Messadeqq, Synthesis and characterization of methylcellulose produced from bacterial cellulose under heterogeneous condition. *J. Brazilian Chem. Sco.*, 2015, 26, 167-174.
13. M. Ghanadpour, B., Wicklein, F. Carosio, L. Wågberg All-natural and highly flam-resistant freeze-cast foams based on phosphorylated cellulose nanofibrils. *Nanoscale*, 2018, 10, 4085.
14. T. Saito, I. Shibata, A. Isogai, N. Suguri, N. Sumikwa, Distribution of carboxylic groups introduced into cotton linters by TEMPO-mediated oxidation. *Carbohydr. Poly.*, 2005, 61, 414-419.

15. B. L. Cade-Menum, Characterization of phosphorous in environmental and agricultural samples by ^{31}P nuclear magnetic resonance spectroscopy- *Talanta*, 2005, 66, 359-371.
16. C. Montero, B. Clair, T. Almeras, A. V. D. Lee, J. Gril, Relationships between wood elastic strain under bending and cellulose crystal strain. *Comp. Sci. Technol.*, 2012, 72, 175-181.
17. A. Mautner, K.Y. Lee, T. Tammelin, A.P. Mathew, A. Nedoma, K. LI, A. Bismark. Cellulose nanopaper as tight aqueous ultra-filtration membranes. *React. Fun. Poly.*, 2015, 86, 209-214.
18. Z. Karim, D. Georgouvelas, A. Svedberg. A. P. Mathew Pilot scale engineering of microfibrillated cellulose (MFC) flat sheet membranes for removal of changed water pollutants. *Carbohy. Poly.*, (2020) (submitted)
19. A. C. F. Ribeiro, M. C. F. Barros, L. Verissimo, C. Santos, Diffusion coefficients of paracetamol in aqueous solutions. *J. Chem. Thermodyn.*, 2012, 54, 97–99.
20. W. E. Price, Tracer caffeine diffusion in aqueous solutions at 298 K. The effect of caffeine self-association. *J. Chem. Soc. Faraday Trans. I Phys. Chem. Condens. Phases*, 1989, 85, 415–419.
21. P. Liu, H. Sehaqui, P. Tingaut, A. Wichser, K. Oksman, A. P. Mathew, Cellulose and chitin nanomaterials for capturing silver ions (Ag^+) from water via surface adsorption. *Cellulose*, 2014, **21**, 449-461.
22. P. Liu, P. F. Borrell, M. Bozic, V. Kokol, K. Oksman, A. P. Mthew, Nanocellulose and their phosphorelated derivatives for selective adsorption of Ag^+ , Cu^{2+} and Fe^{3+} from industrial effluents. *J. Hazar. Mat.*, 2015, **294**, 177-185.
23. H. Sehaqui, U. P. de Larraya, P. Liu, N. Pfenninger, A. P. Mathew, T. Zimmermann, P. Tingaut, Enhancing adsorption of heavy metal ions onto biobased nanofibers from waste pulp residues for application in wastewater treatment. *Cellulose*, 2014, **21**, 2831-2844.
24. A. Daochalermwong, N. Chanaka, K. Songsrirote, P. Sittanet, C. Niamnuy, A. Seubsai, Removal of heavy metal ions using celluloses prepared from pineapple leaf fiber. *ACS Omega* 2020, **5**, 5285-5296.

25. L. Zhang, S. Yang, T. Han, L. Zhong, C. Ma, Y. Zhou, X. Han, Improvement of Ag(I) adsorption onto chitosan/triethanolamine composite sorbent by an ion-imprinted technology, *Appl. Surf. Sci.*, 2012, **263**, 696–703.
26. T. Gotoh, K. Matsushima, K.- Kikuchi, Preparation of alginate-chitosan hybrid gel beads and adsorption of divalent metal ions. *Chemosphere*, 2004, **55**, 135-140.
27. J. Dai, F.L. Ren, C.Y. Tao, Adsorption behavior of Fe(II) and Fe(III) ions on thiourea cross-linked chitosan with Fe(III) as template. *Molecules*, 2012, **17**, 4388–4399.
28. Z. Karim, A. Svedberg, S. Ayub. Role of functional groups in the production and self-assembled microfibrillated cellulose hybrid framework and influence on separation mechanism of dye from aqueous medium. *Int. J. Biol. Macro.*, 2020, **155**, 1541-1552.
29. V. Kokol, V. Vivod, S. Arnus, U. Cernigoj, B. Garlicic, K. Obu-Vazner, B. Neral, A. Mihelic, Zeolite integrated nanocellulose films for removal of loose anionic reactive dye by adsorption vs. filtration mode during textile laundering. *Fiber Polym.*, 2018, **19**, 1556–1566.
30. R. Bhattacharyya, S.K. Ray, Kinetic and equilibrium modeling for adsorption of textile dyes in aqueous solution by carboxymethyl cellulose/poly(acrylamide-co-hydroxyethylmethacrylate) semi-interpenetrating network hydrogel, *Poly. Engineer. Sci.*, 2013, **53**, 2439–2453.
31. K. Xie, W. Zhao, X. He, Adsorption properties of nano-cellulose hybrid containing polyhedral oligomeric silsesquioxane and removal of reactive dyes from aqueous solution, *Carbohydr. Polym.*, 2011, **83**, 1516-1520.
32. H. J. C. Berendsen J. P. M. Postma, W. F. van-Gunsteren, A. DiNola, J. R. Haak Molecular Dynamics with coupling to an external bath *J. Chem. Phys.*, 1984, **81**, 3684-3690.
33. C. Zhu, S. Monti, A. P. Mathew, Cellulose nanofiber–graphene oxide biohybrids: disclosing the self-assembly and copper-ion adsorption using advanced microscopy and ReaxFF simulations. *ACS Nano*, 2018, **12**, 7028-7038.
34. E. J. Baerends ADF, adf2016.106 SCM, Theoretical Chemistry, Vrije Universiteit, Amsterdam, The Netherlands, <http://www.scm.com>